

## Article

# Microstructure and Corrosion Properties of $\text{La}_2\text{Zr}_2\text{O}_7/\text{NiCoAlY}$ Thermal Barrier Coatings Deposited on Inconel 718 Superalloy by Laser Cladding

Kaijin Huang<sup>1,2,3,\*</sup>, Wei Li<sup>2</sup>, Kai Pan<sup>1</sup>, Xin Lin<sup>3</sup> and Aihua Wang<sup>2</sup>

<sup>1</sup> Key Laboratory of Low Dimensional Materials & Application Technology, Xiangtan University, Xiangtan 411105, China; amrp@xtu.edu.cn

<sup>2</sup> State Key Laboratory of Materials Processing and Die & Mould Technology, Huazhong University of Science and Technology, Wuhan 430074, China; liwei990628@hust.edu.cn (W.L.); ahwang@hust.edu.cn (A.W.)

<sup>3</sup> State Key Laboratory of Solidification Processing, Northwestern Polytechnical University, Xi'an 710072, China; xlin@nwpu.edu.cn

\* Correspondence: huangkaijin@hust.edu.cn; Tel.: +86-27-87543676

**Abstract:** In order to improve the seawater corrosion resistance of Inconel 718 superalloy, a  $\text{La}_2\text{Zr}_2\text{O}_7/\text{NiCoCrAlY}$  thermal barrier coating corrosion resistant to 3.5 wt.% NaCl aqueous solution was prepared by laser cladding on Inconel 718 superalloy. X-ray diffraction (XRD), Scanning Electron Microscope (SEM), and electrochemical techniques were used to study the microstructure and the corrosion performance of the coating in 3.5 wt.% NaCl solution. The results show that the thermal barrier coating is mainly composed of primary  $\text{La}_2\text{Zr}_2\text{O}_7$  phase and  $\gamma + \text{laves}/\delta$  phase eutectic structure. The corrosion potential and corrosion current of the coating in 3.5 wt.% NaCl solution are higher and lower than that of the Inconel 718 substrate, respectively, indicating that the corrosion performance of the coating is better than that of the Inconel 718 substrate. The presence of  $\text{La}_2\text{Zr}_2\text{O}_7$  phase in the thermal barrier coating is the main reason for its corrosion resistance to 3.5 wt.% NaCl solution.

**Keywords:** laser-cladding;  $\text{La}_2\text{Zr}_2\text{O}_7/\text{NiCoCrAlY}$  thermal barrier coating; Inconel 718 superalloy; corrosion resistance



**Citation:** Huang, K.; Li, W.; Pan, K.; Lin, X.; Wang, A. Microstructure and Corrosion Properties of  $\text{La}_2\text{Zr}_2\text{O}_7/\text{NiCoAlY}$  Thermal Barrier Coatings Deposited on Inconel 718 Superalloy by Laser Cladding. *Coatings* **2021**, *11*, 101. <https://doi.org/10.3390/coatings11010101>

Received: 23 December 2020

Accepted: 13 January 2021

Published: 18 January 2021

**Publisher's Note:** MDPI stays neutral with regard to jurisdictional claims in published maps and institutional affiliations.



**Copyright:** © 2021 by the authors. Licensee MDPI, Basel, Switzerland. This article is an open access article distributed under the terms and conditions of the Creative Commons Attribution (CC BY) license (<https://creativecommons.org/licenses/by/4.0/>).

## 1. Introduction

It is well-known that thermal barrier coating (TBC) is widely used in aircraft engines, turbines, and turbine blades to protect the high-temperature alloy substrate from high-temperature oxidation and corrosion, and play a role in heat insulation, increasing engine inlet temperature and engine thrust-to-weight ratio. At present, the most common thermal barrier coatings are composed of bond coat and ceramic working layer. Among them, the bond coat material is usually  $\text{MCoCrAlY}$  ( $\text{M} = \text{Ni}$  and/or  $\text{Co}$ ), and the working layer material is mainly ceramics based on 8 wt.%  $\text{Y}_2\text{O}_3$  stable  $\text{ZrO}_2$  (8YSZ) [1–4]. However, 8YSZ coating cannot be applied for a long time under high temperature conditions above 1200 °C, the reason is that when the long-term service temperature is higher than 1200 °C, YSZ will undergo phase transition ( $t\text{-ZrO}_2 \rightarrow t\text{-ZrO}_2 + c\text{-ZrO}_2$ ) and sintering, accompanied by thermal physical and mechanical property degradation, strain tolerance reduction, and crack generation, and eventually lead to coating failure [2,5]. Therefore, in order to meet the higher service temperature requirements of aircraft engines, turbines and turbine blades, it is urgent to develop new ceramic coatings for ultra-high temperature and high thermal insulation thermal barrier. However, as a thermal barrier coating ceramic layer material, it is required to have high melting point, low thermal conductivity, high temperature phase stability, chemical stability, corrosion resistance, thermal expansion coefficient to match the thermal expansion coefficient of the substrate, strong bonding strength with the

metal substrate, good sintering resistance, and other properties. At present,  $\text{La}_2\text{Zr}_2\text{O}_7$  is a new thermal barrier coating ceramic material that can basically meet the performance requirements, and its long-term use temperature can exceed  $1300\text{ }^\circ\text{C}$  [2,6,7].

On the other hand, the current commonly used methods for preparing thermal barrier coatings mainly include plasma spraying and electron beam-physical vapor deposition [1]. The former is easy to operate and cheap, but the adhesion between coating and substrate is not strong, the coating microstructure is lamellar and there is a large porosity. The latter coating microstructure is columnar, coating performance is better than the former, but the equipment is expensive. Therefore, a new thermal barrier coating preparation method, laser cladding method [8–12], has been developed. The coating prepared by this method has fine grain microstructure, strong adhesion between coating and substrate, better coating performance than plasma spraying method, close to electron beam-physical vapor deposition method, and easy to realize automation.

To our best knowledge, there are no other literature reports on the preparation of  $\text{La}_2\text{Zr}_2\text{O}_7$  thermal barrier coating by laser cladding except for our report [9]. However, there have been a large number of literature reports on the preparation of other thermal barrier coatings by laser cladding [8,10–12] and the preparation of  $\text{La}_2\text{Zr}_2\text{O}_7$  thermal barrier coatings by plasma spraying [13–16] and electron beam-physical vapor deposition [17–21]. In addition, there are a large number of literature reports on the corrosion performance of  $\text{La}_2\text{Zr}_2\text{O}_7$  thermal barrier coatings under oxygen [9,16,20,21], molten salts or oxides (such as  $\text{Na}_2\text{SO}_4$ ,  $\text{V}_2\text{O}_5$ , etc.) [4,22–24],  $\text{CaO-MgO-Al}_2\text{O}_3\text{-SiO}_2$  (CMAS) [4,25–27], simulated rain water after CMAS corrosion [28], and high-temperature water vapor [4,29], etc., but there are few literature reports on the corrosion performance of  $\text{La}_2\text{Zr}_2\text{O}_7$  thermal barrier coating in seawater corrosive medium [30]. Considering that aircraft engines, turbines and turbine blades may be stored in a marine environment [28], it is necessary to study the corrosion resistance of  $\text{La}_2\text{Zr}_2\text{O}_7$  thermal barrier coating in this case.

In this paper, a  $\text{La}_2\text{Zr}_2\text{O}_7$  thermal barrier coating containing NiCoCrAlY bond coat was prepared on Inconel 718 superalloy with inner layer of NiCoCrAlY powder and outer layer of  $\text{La}_2\text{Zr}_2\text{O}_7$  powder by laser cladding. The microstructure characteristics and corrosion properties of the coating in 3.5 wt.% NaCl solution were studied. The results show that the corrosion performance of the  $\text{La}_2\text{Zr}_2\text{O}_7$  thermal barrier coating containing NiCoCrAlY bond coat is better than that of the Inconel 718 substrate.

## 2. Materials and Methods

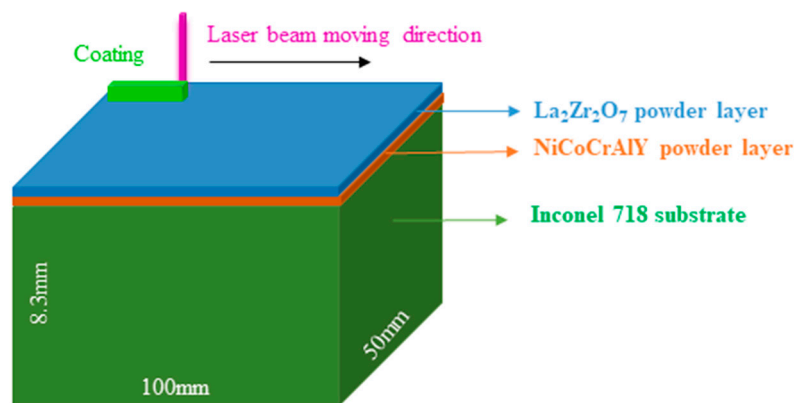
Inconel 718 (supplied by Shanghai Tengsi Special Alloy Company Limited, Shanghai, China) was selected as the substrate material, its size was  $100\text{ mm} \times 50\text{ mm} \times 8\text{ mm}$ , and its chemical composition is shown in Table 1. The bond coat powder was NiCoCrAlY, with a purity of 99.0 wt.% and a particle size of  $37\text{--}75\text{ }\mu\text{m}$ , and its chemical composition is shown in Table 2.  $\text{La}_2\text{Zr}_2\text{O}_7$  was selected as a thermal barrier coating ceramic powder with a purity of 99.5 wt.% and a particle size of  $37\text{--}75\text{ }\mu\text{m}$ . Figure 1 is the schematic diagram of the pre-set powder layer before laser cladding (the second powder layer was applied only after the first powder layer was naturally dry). The binder for the pre-set powder was 4% Polyvinyl Alcohol (PVA) solution. Among them, the thickness of NiCoCrAlY powder layer was about 0.1 mm, the thickness of  $\text{La}_2\text{Zr}_2\text{O}_7$  powder layer was about 0.2 mm, and the total thickness of the preset powder layer was about 0.3 mm. The LDF8000-60 semiconductor laser produced by Laserline (Augsburg, Germany) was used for laser cladding. The optimized laser cladding parameters were as follows: laser power  $P = 3.5\text{ kW}$ , laser scanning speed  $V = 10\text{ mm/s}$ , square laser spot area  $S = 5 \times 5\text{ mm}^2$ , laser spot overlap rate  $f = 30\%$ , and the Ar gas flow with protective effect was  $16\text{ L/min}$ .

**Table 1.** Chemical composition of the Inconel 718 superalloy.

Element	Cr	Ni	Nb	Al	Co	Mo	Ti	C	Fe
wt.%	18.8	52.7	5.3	0.5	0.02	2.9	0.9	0.03	Bal.

**Table 2.** Chemical composition of the NiCoCrAlY powder.

Element	Ni	Co	Cr	Al	Y
wt.%	43.0	24.0	20.0	12.0	1.0

**Figure 1.** Schematic diagram of pre-set powder layer before laser cladding.

The coated samples were cut into small samples of 8 mm × 8 mm × 8 mm by wire cutting method, which were used to study the microstructure and corrosion resistance of the coating. It should be pointed out that both the laser clad coating and Inconel 718 samples have undergone processes such as silicon carbide sandpaper grinding, diamond abrasive paste polishing, running water washing, cold air drying, and putting into a dryer for standby use. The phase analysis of the coating was performed on X' Pert PRO X-ray diffractometer manufactured by PANalytical B.V. (Almelo, The Netherlands). The test parameters were as follows: Cu target was used, start position 2θ was 20.0197°, end position 2θ was 89.9467°, step size 2θ was 0.0390°, scan type was continuous, divergence slit size was 0.4354°. The microstructure of the cross-section coating etched with an aqua regia was observed and analyzed by Quanta 650 scanning electron microscope with energy-dispersive X-ray spectroscopy produced by FEI (Quanta 650 FEG, Eindhoven, The Netherlands).

The electrodynamic polarization curves of the coating and Inconel 718 substrate were completed on the CS350H electrochemical workstation manufactured by Wuhan Corrtest Instruments Co. Ltd. (Wuhan, China) A standard three-electrode test system was used in the experiment, with the coating as the working electrode, platinum electrode as the auxiliary electrode and saturated calomel electrode as the reference electrode. The effective exposure area of the coating and Inconel 718 substrate samples was 64 mm<sup>2</sup>. 3.5 wt.% NaCl aqueous solution was used for corrosion tests. Soak the sample for 30 min before starting the measurement. The parameters used in the measurement were as follows: the scanning speed was 1 mV/s, and the scanning range was −2.5 to 1.0 V.

The surface morphologies of the corroded specimens were observed using a Quanta 650 scanning electron microscope with an energy spectrum (FEI Quanta 650 FEG, Eindhoven, The Netherlands).

### 3. Results and Discussion

#### 3.1. Microstructure

Figure 2 shows the SEM morphology of laser clad cross-section coating. Figure 3 shows the XRD patterns of the laser clad coating. In Table 3, the results of the elemental EDS analysis of the laser clad coating at different positions are given. It can be seen from Figure 2a that the laser clad coating is composed of a laser modified layer and a substrate, of which the thickness of the laser modified layer is about 1738–2024 μm (The measurement method provided in literature [31] was adopted.). According to Figure 2b–e and Table 3, the laser modified layer is composed of the La<sub>2</sub>Zr<sub>2</sub>O<sub>7</sub> layer and the laser alloying layer, of

which the thickness of  $\text{La}_2\text{Zr}_2\text{O}_7$  layer is about 34–47  $\mu\text{m}$ . The interface of  $\text{La}_2\text{Zr}_2\text{O}_7$  layer and the laser alloying layer is well combined without cracks and pores. The alloying layer is mainly composed of  $\gamma$  + Laves/ $\delta$  phase eutectic structure. The reasons are as follows:

- (1) Table 3 shows that EDS results at position D are mainly composed of O, Zr, and La. Combined with XRD calibration results in Figure 3, it can be seen that the coating is mainly  $\text{La}_2\text{Zr}_2\text{O}_7$  (JCPDS 01-073-0444) phase. The other small amounts of Al, Ni, Nb, Cr, Ti, Fe, Co, Mo, and Y in position D should come from the laser-heated molten bond coat NiCoCrAlY powder and partially melted Inconel 718 substrate. This is caused by the rapid laser heating and solidification during laser cladding, and the mixed alloy elements have no time to separate.
- (2) Table 3 shows that the Nb content of Spot3 and Spot6 exceed 10 at.% and they are probably Laves phases. Since Laves phase is generally  $\text{A}(\text{Fe}, \text{Ni}, \text{Cr})_2\text{B}(\text{Nb}, \text{Mo}, \text{Ti})$  type, they might be  $\text{Cr}_2\text{Nb}$  phase in combination with EDS results of Spot3 and Spot6. This is consistent with the results reported in literature [32–35].
- (3) Table 3 shows that the Nb content of Spot2 and Spot4 is 8.51 at.% and 5.62 at.%, respectively. They are probably  $\delta$  phase ( $\text{Ni}_3\text{Nb}$ ). The reason is that the solidification temperature of  $\delta$  phase is 860–995  $^\circ\text{C}$  and Nb concentration requirement is 6–8 at.% [35]. This is consistent with the results reported in literature [32].
- (4) Table 3 shows that Fe, Ni and Cr contents in Spot1, Spot5, and Spot7 are dominant, which should be  $\gamma$  phase ((Fe, Ni, and Cr) solid solution).
- (5) A large number of literature studies have shown [36–38] that the solidification process sequence of Inconel 718 substrate is  $\text{L} \rightarrow \gamma \rightarrow \gamma + \text{NbC}$  (high temperature) eutectic reaction  $\rightarrow \gamma + \text{laves}$  (low temperature) eutectic reaction. According to EDS results in Table 3, in the laser cladding process, the chemical composition of the laser heating melted preset powder layer, and partially melted Inconel 718 substrate deviated from the chemical composition of Inconel 718 substrate due to mixing, but the degree of deviation should be small, because the chemical composition of the added NiCoCrAlY bond coat powder is basically the composition of Inconel 718 substrate. Therefore, we believe that the solidification process of the laser modified layer is as follows: The high melting point  $\text{La}_2\text{Zr}_2\text{O}_7$  (2300  $^\circ\text{C}$ ) solidified first, and the remaining alloy liquid followed the solidification sequence of Inconel 718 alloy:  $\text{L} \rightarrow \gamma \rightarrow (\gamma + \text{NbC})$  eutectic reaction  $\rightarrow (\gamma + \text{Laves})$  eutectic reaction. In other words, the solidification of remaining alloy liquid was mainly caused by  $\text{L} \rightarrow \gamma$  reaction at the beginning. As time went on, Nb, Mo, Ti, C, and other elements were enriched between dendrites, leading to the eutectic reaction  $\text{L} \rightarrow (\gamma + \text{NbC})$  and the consumption of a large number of C atoms in the alloy. As the  $\text{L} \rightarrow \gamma$  reaction continued and progressed, further enrichment of the interdendrite liquid solute atoms occurred until the eutectic reaction  $\text{L} \rightarrow (\gamma + \text{Laves})$  occurred and the solidification process was complete. At the same time, due to the characteristics of rapid laser heating and fast solidification, Nb element segregation was serious, and part of the regions with low Nb content generated  $\delta$  phase instead of Laves phase, because Nb content in  $\delta$  phase is usually 6–8 at. %, while Nb content in Laves phase usually exceeds 10 at. % [32–35].

It should be pointed out that there exists a large temperature gradient on the upper and lower surface of the molten pool during the laser action, thus forming an extremely steep surface tension, which causes a strong convection in the molten pool, and the convection in the molten pool can produce a strong stirring force, so that the liquid metal in the molten pool mixed evenly. The convection in the molten pool mainly comes from three aspects: First, the convection in the molten pool comes from the energy distribution of the laser beam, and the Gaussian laser beam used in this experiment can cause severe convection in the molten pool. The second factor is the protective gas that blows out to prevent the oxidation of liquid metals at high temperature. This high-pressure protective gas produces a stirring effect that promotes the diffusion of the liquid metal. Thirdly, at high temperature, the liquid metal expands when heated to form a certain density difference in the molten pool, thus generating buoyancy in the pool, the existence of which will cause the natural

convection of the melt [39]. It is these three factors that make the multi-layer preset powder mode also form the microstructure obtained by the single-layer preset powder mode, thus reducing the mixing time of powder, and improving the production efficiency.

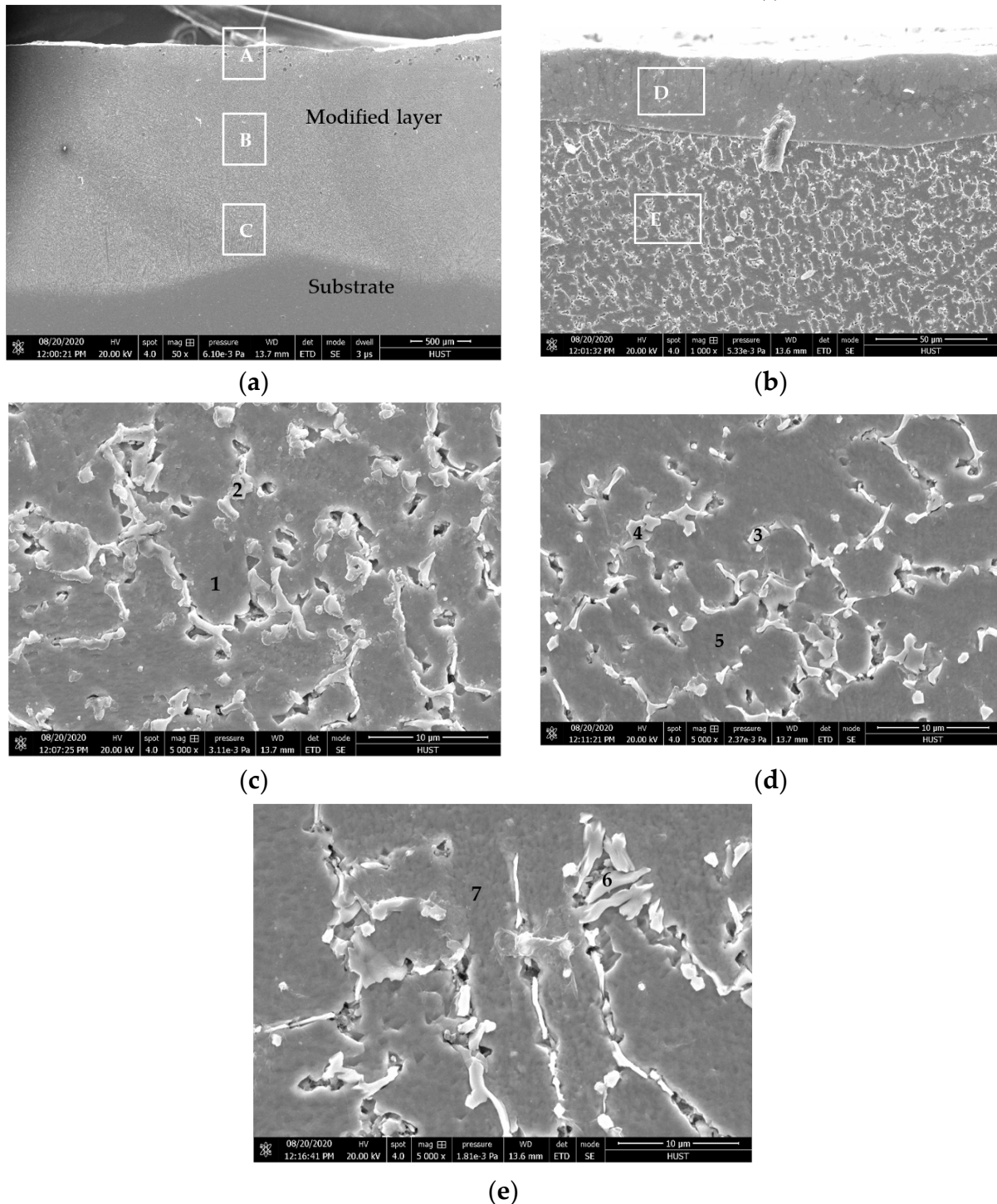


**Figure 2.** SEM images of the laser clad  $\text{La}_2\text{Zr}_2\text{O}_7/\text{NiCoCrAlY}$  coating: (a) whole, (b) at position A, (c) at position E, (d) at position B, (e) at position C. (A, B and C represent the top, middle and bottom of the coating, respectively. D and E represent the locally amplified  $\text{La}_2\text{Zr}_2\text{O}_7$  layer and alloying layer at position A, respectively. Numbers 1–7 represent substrates or particles at corresponding positions of the coating.).

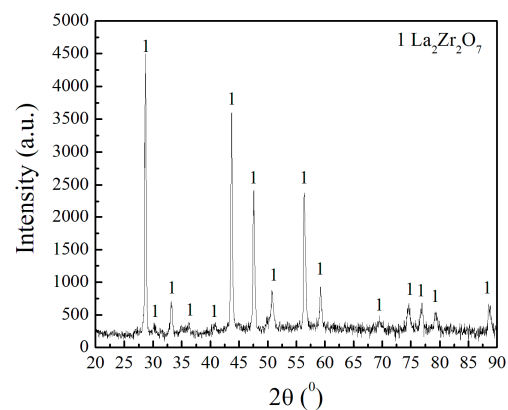


Figure 3. XRD patterns of the laser clad coating.

Table 3. EDS results of the coating at different positions of Figure 2 (at.%).

Element	O	Zr	La	Ni	Nb	Cr	Ti	Fe	Al	Co	Mo	Y	Possible Phase
Area D	58.2	20.4	15.6	0.1	0.0	0.4	0.8	0.1	3.5	0.0	0.0	0.9	La <sub>2</sub> Zr <sub>2</sub> O <sub>7</sub>
Spot1	11.5	4.1	0.2	32.2	0.4	18.1	0.4	30.5	1.9	0.1	0.5	0.1	γ
Spot2	21.1	5.2	0.2	22.8	8.5	14.8	1.8	21.2	2.8	0.1	1.0	0.5	δ
Spot3	28.0	4.9	0.2	13.6	11.0	19.4	1.2	14.6	2.1	0.2	4.3	0.5	Laves
Spot4	19.9	4.6	0.2	22.4	5.6	19.8	1.0	20.2	2.6	0.2	3.0	0.5	δ
Spot5	12.2	4.3	0.2	31.1	0.5	18.1	0.6	29.9	2.2	0.1	0.6	0.2	γ
Spot6	28.7	5.3	0.2	13.6	10.9	18.8	0.9	14.4	2.2	0.2	4.3	0.5	Laves
Spot7	13.3	4.5	0.2	31.2	0.6	18.0	0.5	28.7	2.1	0.0	0.7	0.2	γ

Finally, combining the results of Figures 2 and 3 and Table 3, we give a schematic diagram of the phase distribution in different regions of the laser modified layer, as shown in Figure 4.

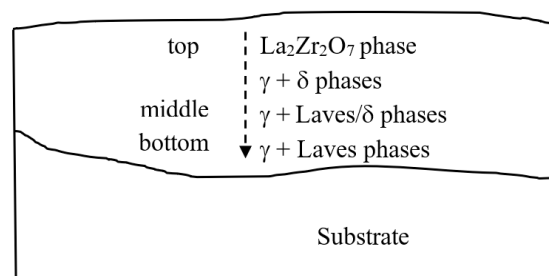
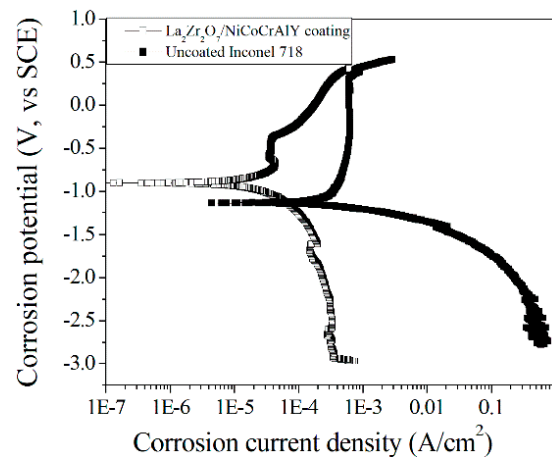


Figure 4. Schematic diagram of phase distribution in different areas of the laser modified layer.

### 3.2. Corrosion Properties

Figure 5 shows the potentiodynamic polarization curve of laser clad La<sub>2</sub>Zr<sub>2</sub>O<sub>7</sub>/NiCoCrAlY coating and Inconel 718 substrate in 3.5 wt.% NaCl aqueous solution. Table 4 shows the corrosion potential and current of the laser clad coating and Inconel 718 substrate in 3.5 wt.% NaCl aqueous solution. It can be seen from Figure 5 and Table 4 that the corrosion potential of laser clad coating is 0.22 V higher than that of Inconel 718 substrate, and the corrosion current is about one eleventh of that of Inconel 718 substrate. According to the principle of “the higher the corrosion potential of the material, the smaller the corrosion current and the better the corrosion resistance”, the corrosion resistance of laser clad coating in 3.5 wt.% NaCl aqueous solution is better than Inconel 718 substrate. The reason is that the surface layer of laser clad coating (Figures 2b and 3) is mainly composed of dense La<sub>2</sub>Zr<sub>2</sub>O<sub>7</sub> phase, which has excellent corrosion resistance to 3.5 wt.% NaCl aqueous solution [30].



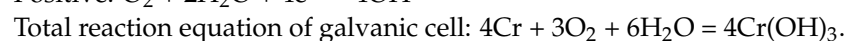
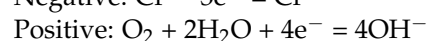
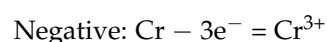
**Figure 5.** Potentiodynamic polarization curve of laser clad  $\text{La}_2\text{Zr}_2\text{O}_7/\text{NiCoCrAlY}$  coating and Inconel 718 substrate in 3.5 wt.% NaCl aqueous solution.

**Table 4.** Corrosion parameters of different samples in 3.5 wt.% NaCl solution.

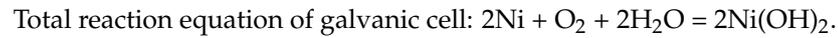
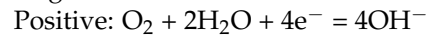
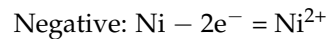
Specimen	$E_{\text{corr}}$ (V)	$I_{\text{corr}}$ ( $\text{A}/\text{cm}^2$ )
Inconel 718	−1.13	$1.44 \times 10^{-4}$
Laser clad coating	−0.91	$1.29 \times 10^{-5}$

It should be noted that the corrosion potential and corrosion current of the pure  $\text{La}_2\text{Zr}_2\text{O}_7$  coating prepared by plasma spraying in 3.5 wt.% NaCl aqueous solution are  $-0.66$  V and  $5.4 \times 10^{-7}$   $\text{A}/\text{cm}^2$ , respectively, as reported in literature [30]. However, in the  $\text{La}_2\text{Zr}_2\text{O}_7$  coating prepared by laser cladding method in this paper, due to a small amount of alloy elements dissolved in the coating (Table 3), the corrosion potential and current are not as good as those reported in literature [30], but they are still better than those of Inconel 718 substrate (Table 4). This indicates that the  $\text{La}_2\text{Zr}_2\text{O}_7/\text{NiCoCrAlY}$  coating prepared by laser cladding is more resistant to corrosion by 3.5 wt.% NaCl aqueous solution than Inconel 718 substrate. This is also evidenced by the surface morphology after corrosion in Figure 6. It can be seen from Figure 6 that the surface of Inconel 718 substrate is seriously damaged after the corrosion of 3.5 wt.% NaCl aqueous solution (Figure 6a), while the surface of laser clad coating is slightly damaged (Figure 6b). In addition, EDS results in Table 5 show that oxygen elements appear in the surface chemical compositions of both samples after corrosion in 3.5 wt.% NaCl aqueous solution. Combined with the EDS results in Tables 1 and 5 and the SEM morphology after corrosion in Figure 6, it can be seen that in Figure 6a, areas A and B should be the surface of the original Inconel 718 alloy that has not been corroded by 3.5 wt.% NaCl aqueous solution and the exposed surface of Inconel 718 alloy after being corroded by 3.5 wt.% NaCl aqueous solution, respectively. The original  $\text{La}_2\text{Zr}_2\text{O}_7$  coating surface not corroded by 3.5 wt.% NaCl aqueous solution should be at area C in Figure 6b. Among them, the oxygen in the surface of the laser clad coating is mainly from  $\text{La}_2\text{Zr}_2\text{O}_7$  phase, while the oxygen in the corrosion surface of Inconel 718 substrate is mainly from the electrochemical reaction (no oxidation film) or chemical reaction (presence of oxide film) of Cr, Ni, Nb, Al, Co, Mo, Ti, and Fe elements in Inconel 718 substrate in 3.5 wt.% NaCl aqueous solution containing oxygen. The detailed electrochemical or chemical reactions of Inconel 718 substrate are as follows:

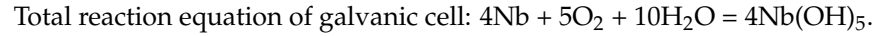
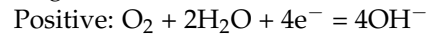
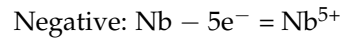
- (1) When there is no oxidation film, the following electrochemical reactions occur in 3.5 wt.% NaCl aqueous solution containing oxygen for Cr, Ni, Nb, Al, Co, Mo, Ti, and Fe elements in Inconel 718 substrate: For Cr element:



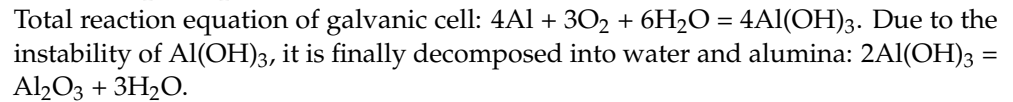
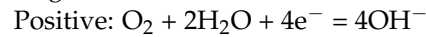
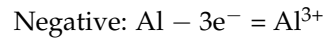
For Ni element:



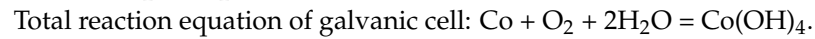
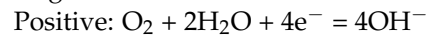
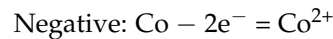
For Nb element:



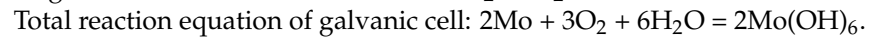
For Al element:



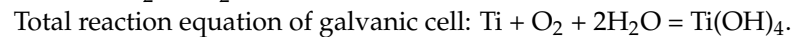
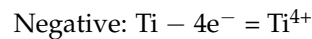
For Co element:



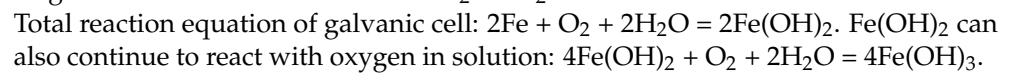
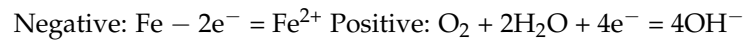
For Mo element:



For Ti element:



For Fe element:



- (2) When there is oxidation film, the following chemical reactions occur in 3.5 wt.% NaCl aqueous solution for Cr, Ni, Nb, Al, Co, Mo, Ti, and Fe elements in Inconel 718 substrate: Generally speaking, all metal elements will form oxide film on their surface at room temperature. Table 6 is the Pilling–Bedworth (P-B) ratio of alloy oxides of Cr, Ni, Nb, Al, Co, Mo, Ti, and Fe. According to the criterion that “the integrity of metal oxide film is a necessary condition for its protection, while the P-B ratio is greater than 1 is a necessary condition for the integrity of metal oxide film”, it can be seen that the oxide film formed by these alloy-elements is complete. However, if the P-B ratio is too large (such as more than 2), the internal stress of the oxide film is large, and the oxide film is easy to break and lose protection or the protection is very poor. Therefore, according to the results in Tables 1 and 6, the presence of Nb and Mo may make the oxidation film formed on the local surface of Inconel 718 substrate worse.

**Table 5.** EDS results of corroded surfaces of the Inconel 718 substrate and the laser clad specimen (at.%).

Samples	Position	O	Zr	La	Al	Nb	Mo	Ti	Cr	Fe	Co	Ni	Y
Inconel 718	Area A	15.0	0.0	0.0	2.2	5.3	0.7	0.7	17.0	39.5	0.2	19.4	0
Inconel 718	Area B	12.5	0.0	0.0	1.4	5.4	0.5	0.9	17.8	38.8	0.4	22.3	0
Inconel 718	Spot 1	10.6	0.0	0.0	1.4	5.3	0.8	0.7	17.6	42.4	0.2	21.0	0
Coating	Area C	61.5	16.0	15.1	4.6	0.2	0.1	0.9	0.5	0.1	0.1	0.2	0.7

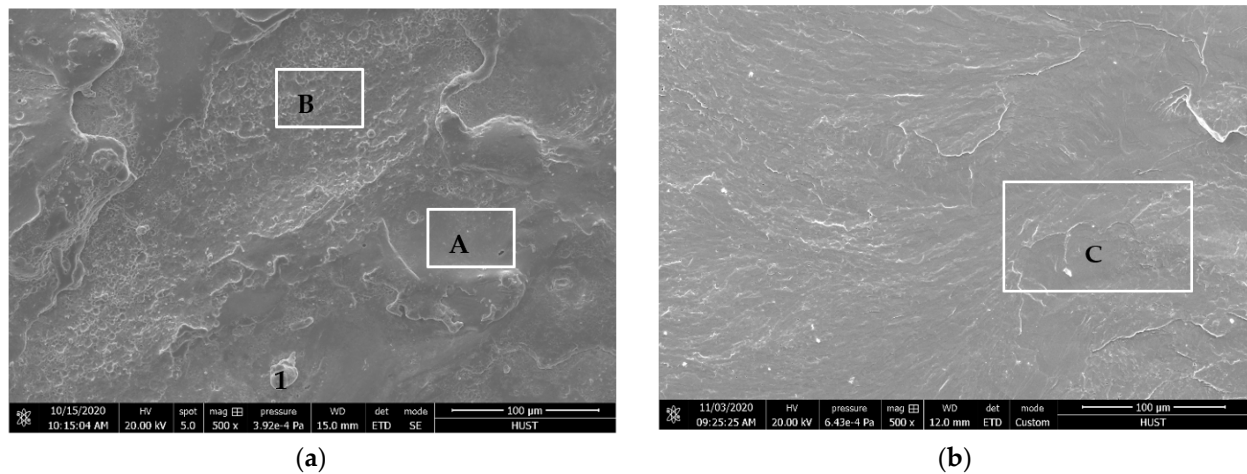
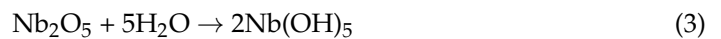


**Figure 6.** SEM images of laser clad  $\text{La}_2\text{Zr}_2\text{O}_7/\text{NiCoCrAlY}$  coating and Inconel 718 substrate after corrosion in 3.5 wt.% NaCl solution: (a) Inconel 718 substrate, (b) laser clad coating. (A, B, and C represent the different positions of the corroded specimen.)

**Table 6.** Pilling–Bedworth ratios of different metal oxides [40].

Metal	Cr	Ni	Co	Fe	Fe	Ti	Nb	Al	Mo
oxide	$\text{Cr}_2\text{O}_3$	$\text{NiO}$	$\text{CoO}$	$\text{FeO}$	$\text{Fe}_2\text{O}_3$	$\text{TiO}_2$	$\text{Nb}_2\text{O}_5$	$\text{Al}_2\text{O}_3$	$\text{MoO}_3$
P-B ratio	2.07	1.65	1.86	1.70	2.14	1.73	2.68	1.28	3.4

On the one hand, all the surface metal oxide films will react with the water in 3.5 wt.% NaCl aqueous solution as follows:



On the other hand, due to the presence of  $\text{Cl}^-$  ions with a small radius in the NaCl corrosion solution,  $\text{Cl}^-$  ions will adsorb and penetrate into the metal surface oxidation film and diffuse into the interior and have a chemical reaction with the internal metal (see Equations (10)–(17)), thus reducing the protective effect of the outermost metal oxidation film and increasing the corrosion rate of the Inconel 718 substrate. On the contrary, since  $\text{La}_2\text{Zr}_2\text{O}_7$  is oxygen non-permeable material [2,7], and the radius of  $\text{O}^{2-}$  ion is 140 pm, and the radius of  $\text{Cl}^-$  ion is 181 pm,  $\text{Cl}^-$  cannot penetrate the dense  $\text{La}_2\text{Zr}_2\text{O}_7$  coating. Therefore, the laser clad coating is more resistant to corrosion by 3.5 wt.% NaCl aqueous solution than Inconel 718 substrate.





In conclusion, no matter whether oxidation film is formed on the surface of Inconel 718 substrate, chemical reaction (oxidation film exists), or electrochemical reaction (no oxidation film exists) will occur in 3.5 wt.% NaCl aqueous solution, thus leading to corrosion of Inconel 718 substrate. On the contrary, since  $\text{Cl}^{-}$  ions could not penetrate the dense  $\text{La}_2\text{Zr}_2\text{O}_7$  coating prepared by laser cladding, the corrosion resistance of the coating in 3.5 wt.% NaCl aqueous solution is superior to that of the Inconel 718 substrate.

#### 4. Conclusions

In order to improve the seawater corrosion resistance of aircraft engines, turbines, and turbine blades, a  $\text{La}_2\text{Zr}_2\text{O}_7/\text{NiCoCrAlY}$  coating was prepared by using the pre-set powder layer method and laser cladding, and the following two main conclusions are drawn:

- (1) The outermost layer of the coating is  $\text{La}_2\text{Zr}_2\text{O}_7$  layer, and the secondary layer is mainly composed of  $\gamma + \text{laves}/\delta$  phase eutectic structure.
- (2) The corrosion resistance of the coating is superior to that of Inconel 718 substrate in 3.5 wt.% NaCl aqueous solution, and the presence of  $\text{La}_2\text{Zr}_2\text{O}_7$  phase is the main reason for the improvement of the corrosion resistance of the coating.

**Author Contributions:** Investigation—K.H., W.L., K.P., X.L., and A.W.; writing—original draft preparation, W.L.; writing—review and editing, K.H. All authors have read and agreed to the published version of the manuscript.

**Funding:** This work was supported by the Open Project Program (No. KF20180201) of Key Laboratory of Low Dimensional Materials and Application Technology, Ministry of Education, Xiangtan University, and the Fund (Grant No. SKLSP201913) of the State Key Laboratory of Solidification Processing in NWPU.

**Data Availability Statement:** The data of this study are available from the corresponding author upon reasonable request.

**Acknowledgments:** The authors are also grateful to the Analytical and Testing Center of Huazhong University of Science and Technology.

**Conflicts of Interest:** The authors declare no conflict of interest.

#### References

1. Padture, N.P.; Gell, M.; Jordan, E.H. Materials science-thermal barrier coatings for gas turbine engine applications. *Science* **2002**, *296*, 280–284. [[CrossRef](#)] [[PubMed](#)]
2. Cao, X.Q.; Vassen, R.; Stoeber, D. Ceramic materials for thermal barrier coatings. *J. Eur. Ceram. Soc.* **2004**, *24*, 1–10. [[CrossRef](#)]
3. Evans, A.G.; Mumm, D.R.; Hutchinson, J.W.; Meier, G.H.; Pettit, F.S. Mechanisms controlling the durability of thermal barrier coatings. *Prog. Mater. Sci.* **2001**, *46*, 505–553. [[CrossRef](#)]
4. Chen, H.F.; Zhang, C.; Liu, Y.C.; Song, P.; Li, W.X.; Yang, G.; Liu, B. Recent progress in thermal/environmental barrier coatings and their corrosion resistance. *Rare Metal.* **2020**, *39*, 498–512. [[CrossRef](#)]
5. Clarke, D.R.; Levi, C.G. Materials design for the next generation thermal barrier coatings. *Annu. Rev. Mater. Res.* **2003**, *33*, 383–417. [[CrossRef](#)]
6. Vassen, R.; Cao, X.Q.; Tietz, F.; Basu, D.; Stover, D. Zirconates as new materials for thermal barrier coatings. *J. Am. Ceram. Soc.* **2000**, *83*, 2023–2028. [[CrossRef](#)]
7. Zhang, J.; Guo, X.Y.; Jung, Y.G.; Li, L.; Knapp, J. Lanthanum zirconate based thermal barrier coatings: A review. *Surf. Coat. Technol.* **2017**, *323*, 18–29. [[CrossRef](#)]

8. Zheng, H.Z.; Zhou, P.F.; Li, G.F.; Peng, P. Cyclic oxidation behavior of NiCoCrAlY/YSZ@Ni composite coatings fabricated by laser cladding. *J. Iron Steel Res. Int.* **2020**, *27*, 1226–1235. [[CrossRef](#)]
9. Huang, K.J.; Li, W.; Pan, K.; Lin, X.; Wang, A.H. High temperature oxidation and thermal shock properties of La<sub>2</sub>Zr<sub>2</sub>O<sub>7</sub> thermal barrier coatings deposited on nickel-based superalloy by laser-cladding. *Coatings* **2020**, *10*, 370. [[CrossRef](#)]
10. Cui, J.; Zhai, W.; Lu, M.K.; Zhang, H.; Pang, M.; Yang, G.F. Experimental study of the microscopic characteristics of Ti-based laser cladding Ti+7YSZ composite thermal barrier coatings. *Optik* **2020**, *208*, 164087. [[CrossRef](#)]
11. Soleimanipour, Z.; Baghshahi, S.; Shoja-razavi, R. Improving the thermal shock resistance of thermal barrier coatings through formation of an in situ YSZ/Al<sub>2</sub>O<sub>3</sub> composite via laser cladding. *J. Mater. Eng. Perform.* **2017**, *26*, 1890–1899. [[CrossRef](#)]
12. Renna, G.; Leo, P.; Cerri, E.; Zanon, G.P. Thermal shock behavior of CoCrAlTaY coatings on a Ni-base superalloy. *Metall. Ital.* **2015**, *7–8*, 33–41.
13. Cihan, O.; Temizer, I.; Gok, M.G.; Karabas, M. Investigation of the effect of rare earth doped La<sub>2</sub>Zr<sub>2</sub>O<sub>7</sub> based thermal barrier coating on performance and combustion characteristics of DI diesel engine. *Surf. Coat. Technol.* **2020**, *403*, 126437. [[CrossRef](#)]
14. Satpathy, R.; Rani, S.; Alam, Z.; Besra, L. Effectiveness of lanthanum zirconate and yttria stabilized zirconia freestanding APS thermal barrier coatings against natural CMAS attack at high temperatures. *Mater. High Temp.* **2020**, *37*, 416–424. [[CrossRef](#)]
15. Bobzin, K.; Zhao, L.D.; Wietheger, W.; Konigstein, T. Key influencing factors for the thermal shock resistance of La<sub>2</sub>Zr<sub>2</sub>O<sub>7</sub>-based multilayer TBCs. *Surf. Coat. Technol.* **2020**, *396*, 125951. [[CrossRef](#)]
16. Wang, R.; Dong, T.S.; Di, Y.L.; Wang, H.D.; Li, G.L.; Liu, L. High temperature oxidation resistance and thermal growth oxides formation and growth mechanism of double-layer thermal barrier coatings. *J. Alloys Compd.* **2019**, *798*, 773–783. [[CrossRef](#)]
17. Bobzin, K.; Broegelmann, T.; Kalscheuer, C.; Yildirim, B.; Welters, M. Correlation of thermal characteristics and microstructure of multilayer electron beam physical vapor deposition thermal barrier coatings. *Thin Solid Films* **2020**, *707*, 138081. [[CrossRef](#)]
18. Karaoglanli, A.C.; Doleker, K.M.; Ozgurluk, Y. Interface failure behavior of yttria stabilized zirconia (YSZ), La<sub>2</sub>Zr<sub>2</sub>O<sub>7</sub>, Gd<sub>2</sub>Zr<sub>2</sub>O<sub>7</sub>, YSZ/La<sub>2</sub>Zr<sub>2</sub>O<sub>7</sub> and YSZ/Gd<sub>2</sub>Zr<sub>2</sub>O<sub>7</sub> thermal barrier coatings (TBCs) in thermal cyclic exposure. *Mater. Charact.* **2020**, *159*, 110072. [[CrossRef](#)]
19. Jesuraj, S.A.; Kuppusami, P.; Kumar, S.A.; Panda, P.; Udaiyappan, S. Investigation on the effect of deposition temperature on structural and nanomechanical properties of electron beam evaporated lanthanum zirconate coatings. *Mater. Chem. Phys.* **2019**, *236*, 121789. [[CrossRef](#)]
20. Doleker, K.M.; Ozgurluk, Y.; Karaoglanli, A.C. Isothermal oxidation and thermal cyclic behaviors of YSZ and double-layered YSZ/La<sub>2</sub>Zr<sub>2</sub>O<sub>7</sub> thermal barrier coatings (TBCs). *Surf. Coat. Technol.* **2018**, *351*, 78–88. [[CrossRef](#)]
21. Bobzin, K.; Broegelmann, T.; Kalscheuer, C.; Yildirim, B.; Welters, M. Thermal cycling and isothermal oxidation behavior of quadruple EB-PVD thermal barrier coatings. *Mater. Wiss. Werkst.* **2017**, *48*, 502–518. [[CrossRef](#)]
22. Song, D.; Song, T.; Paik, U.; Lyu, G.; Jung, Y.G. Hot corrosion behavior in thermal barrier coatings with heterogeneous splat boundary. *Corros. Sci.* **2020**, *163*, 108225. [[CrossRef](#)]
23. Jasik, A.; Moskal, G.; Jucha, S.; Kuligowski, K. Surface condition of La<sub>2</sub>Zr<sub>2</sub>O<sub>7</sub> based TBC system after hot corrosion in molten sulfate Na<sub>2</sub>SO<sub>4</sub> salts. *Ochrona Przed Korozja* **2019**, *62*, 82–85. [[CrossRef](#)]
24. Zhu, C.H.; Yang, L.; Zhang, C.G.; Yang, G.; Chen, H.F.; Li, Q.; Li, F.Z.; Gao, Y.F.; Liu, B. Influence of composition on molten sulfate-vanadate salt corrosion resistance of lanthanum zirconate coatings. *Ceram. Int.* **2018**, *44*, 22911–22918. [[CrossRef](#)]
25. Lyu, G.; Song, D.; Choi, B.G.; Jung, Y.G. Infiltration behavior of CMAS in LZ-YSZ composite thermal barrier coatings. *JOM* **2020**. [[CrossRef](#)]
26. Zhang, C.G.; Zhao, J.L.; Yang, L.; Zhou, Y.C.; Wang, Q.F.; Chen, H.F.; Yang, G.; Gao, Y.F.; Liu, B. Preparation and corrosion resistance of nonstoichiometric lanthanum zirconate coatings. *J. Eur. Ceram. Soc.* **2020**, *40*, 3122–3128. [[CrossRef](#)]
27. Schulz, U.; Braue, W. Degradation of La<sub>2</sub>Zr<sub>2</sub>O<sub>7</sub> and other novel EB-PVD thermal barrier coatings by CMAS (CaO-MgO-Al<sub>2</sub>O<sub>3</sub>-SiO<sub>2</sub>) and volcanic ash deposits. *Surf. Coat. Technol.* **2013**, *235*, 165–173. [[CrossRef](#)]
28. Wang, R.; Dong, T.S.; Wang, H.D.; Di, Y.L.; Li, G.L.; Feng, Y. CMAS corrosion resistance in high temperature and rainwater environment of double-layer thermal barrier coatings modified by rare earth. *Ceram. Int.* **2019**, *45*, 17409–17419. [[CrossRef](#)]
29. Jian, Z.; Wei, L.; Song, W.; Wang, S.X. Electrophoretic deposition of La<sub>2</sub>Zr<sub>2</sub>O<sub>7</sub> coatings in non-aqueous media on C<sub>f</sub>/SiC substrate. *Surf. Coat. Technol.* **2015**, *278*, 80–86. [[CrossRef](#)]
30. Sun, J.; Fu, Q.G.; Yuan, R.M.; Dong, K.Y.; Guo, J.J. Corrosion and thermal cycling behavior of plasma sprayed thermal barrier coatings on die steel. *Mater. Des.* **2017**, *114*, 537–545. [[CrossRef](#)]
31. Huang, B.Z. Research on high temperature properties of laser remelting plasma sprayed ZrO<sub>2</sub>-8%Y<sub>2</sub>O<sub>3</sub> thermal barrier coatings on GH4169 alloy. Master of Thesis, Nanjing University of Aeronautics and Astronautics, Nanjing, China, 2017. (In Chinese).
32. Xi, M.Z.; Zhou, W.; Shang, J.Y.; Lv, C.; Wu, Z.H.; Gao, S.Y. Effect of heat treatment on microstructure and mechanical properties of consecutive point-mode forging and laser rapid forming GH4169 alloy. *Acta Metall. Sin.* **2017**, *53*, 239–247. (In Chinese)
33. Zhang, Y.C.; Li, Z.G.; Nie, P.L.; Wu, Y.X. Effect of heat treatment on niobium segregation of laser-cladded In718 alloy coating. *Metall. Mater. Trans. A* **2013**, *44*, 708–716. [[CrossRef](#)]
34. Long, Y.T.; Nie, P.L.; Li, Z.G.; Huang, J.; Li, X.; Xu, X.M. Segregation of niobium in laser cladding Inconel 718 superalloy. *Trans. Nonferrous Met. Soc.* **2016**, *26*, 431–436. [[CrossRef](#)]
35. Ram, G.D.J.; Reddy, A.V.; Rao, K.P.; Reddy, G.M.; Sundar, J.K.S. Microstructure and tensile properties of Inconel 718 pulsed Nd-YAG laser welds. *J. Mater. Process. Tech.* **2005**, *167*, 73–82.

36. DuPont, J.N.; Robino, C.V.; Michael, J.R.; Notis, M.R.; Marder, A.R. Solidification of Nb-bearing superalloys: Part I. Reaction sequences. *Metall. Mater. Trans. A* **1998**, *29*, 2785–2796. [[CrossRef](#)]
37. Antonsson, T.; Fredriksson, H. The effect of cooling rate on the solidification of INCONEL 718. *Metall. Mater. Trans. B* **2005**, *36*, 85–96. [[CrossRef](#)]
38. Dupont, J.N.; Robino, C.V.; Marder, A.R. Solidification and weldability of Nb-bearing superalloys. *Weld. J.* **1998**, *77*, 417–431.
39. Jackson, M.J.; Robinson, G.M.; Gill, M.D.H.; Neill, W.O. The effect of nozzle design on laser micro-machining of M2 tool steels. *J. Mater. Process. Tech.* **2005**, *160*, 198–212. [[CrossRef](#)]
40. Evans, H.E. Stress effects in high temperature oxidation of metals. *Int. Mater. Rev.* **1995**, *40*, 1–40. [[CrossRef](#)]